Photonic Radio-Frequency Arbitrary Waveform Generation With Maximal Time-Bandwidth Product Capability

Amir Rashidinejad, *Member, IEEE*, and Andrew M. Weiner, *Fellow, IEEE*

(Invited Paper)

***Abstract*—We present an innovative photonic strategy to generate arbitrary microwave and millimeter-wave signals with maximal time-bandwidth product capability and broadly tunable center frequency. The proposed approach incorporates high-resolution pulse shaping, optical interferometry, and the concept of frequency-to-time mapping in order to enable independent control over the temporal amplitude, temporal phase, and center frequency of the generated waveforms. Numerical simulation and experimental results validate that the time-bandwidth product of these pulses is equal to the upper bound set by the number of independent pulse shaper control elements, extending to more than twice that of conventional frequency-to-time mapping techniques. We thus demonstrate a record photonic arbitrary waveform generation time-bandwidth product of ~589. Also, a length 15 Costas sequence realization is implemented to further portray the potentials of this technique. Detailed analysis of the repeatability and stability of these waveforms as well as higher order dispersion compensation is provided.**

***Index Terms*—Microwave generation, millimeter-wave generation, optical pulse shaping, radio frequency photonics.**

I. Introduction

DURING the last couple of decades, the ongoing challenge of radio-frequency arbitrary waveform generation (RF-AWG) in the high-microwave and millimeter-wave (MMW) frequency region has impeded the satisfactory development of many applications within this regime. As a result of the overcongestion of low-frequency bands, successful access to the broad frequency region between 30 and 300 GHz is a fundamental prerequisite in the evolution of a large number of applications, such as high-resolution ranging, electromagnetic imaging, remote sensing and high-speed wireless communications [1]–[5].

Due to the practical limits associated with digital-to-analog converters, the current state-of-the-art electronic RF-AWG technology is confined to waveforms within and below the microwave frequency range. Electronic solutions also suffer from the viewpoint of timing jitter, electromagnetic interference (EMI) and bulkiness. RF-photonic strategies, however, owing to their inherent broadband nature, have proven to be more attractive for microwave (μ-wave), MMW and even sub-Terahertz (sub-THz) generation [6]–[10] with very high signal fidelity.

Many RF-photonic schemes have been developed to generate a wide variety of desirable RF waveforms at high frequencies [10]–[22]. For example, chirped MMW pulse generation has drawn a great deal of research attention in the RF-photonics community [16]–[19]. The key advantage of many of these methods is their ability to generate chirped waveforms with ultra-wide bandwidths across high center frequencies. Another example of RF-photonic waveform generation is the ability to construct frequency-hopped microwave pulses with indefinite record lengths by exploiting the ultrafast switching capability and optical pulse shaping resources available in photonics [20], [21].

Other techniques, on the other hand, are not only aimed at generating specific classes of waveforms, but target the possibility of creating programmable RF waveforms [11]–[15], [20]–[22]. These RF-photonic arbitrary waveform generation schemes allow the user to define, in a reconfigurable manner, any desired RF waveform that could be employed in various applications. Among the many photonic RF-AWG techniques, those relying on optical pulse shaping [23], [24] and the concept of frequency-to-time mapping (FTM) offer better performance in terms of signal fidelity and reconfigurability [12]–[15]. In these techniques, the spectrum of an ultrashort laser pulse is manipulated using various optical pulse shaping configurations. This tailored spectrum is then mapped to the time domain by stretching the optical pulses through a dispersive medium, resulting in a programmable optical intensity profile. The resultant optical intensity can be easily mapped to the RF domain using a high-speed photodetector.

In many applications the ability to generate wideband signals that extend over a long-enough temporal duration is of key importance. This is why most research in the area of RF-AWG has been aimed at the generation of programmable signals exhibiting large time-bandwidth product (TBWP) values [10]. For example, from the point of view of MMW imaging, the key figure-of-merit in evaluating a chirped MMW waveform is its compression ratio, which determines the achievable imaging resolution. This compression ratio is directly proportional to the time-bandwidth product of the utilized chirped signal, i.e., the product of the MMW bandwidth and time duration of the sensing pulse.

Manuscript received January 14, 2014; revised May 23, 2014; accepted June 11, 2014. Date of publication June 17, 2014; date of current version September 1, 2014. This work was supported in part by the Office of the Assistant Secretary of Defense for Research and Engineering under the National Security Science and Engineering Faculty Fellowship program under Grant N00244-09-1-0068 from the Naval Postgraduate School.

The authors are with the School of Electrical and Computer Engineering, Purdue University, West Lafayette, IN 47907-2035 USA (e-mail: arashidi@purdue.edu; amw@ecn.purdue.edu).

Color versions of one or more of the figures in this paper are available online at http:\\ieeexplore.ieee.org.

Digital Object Identifier 10.1109/JLT.2014.2331491

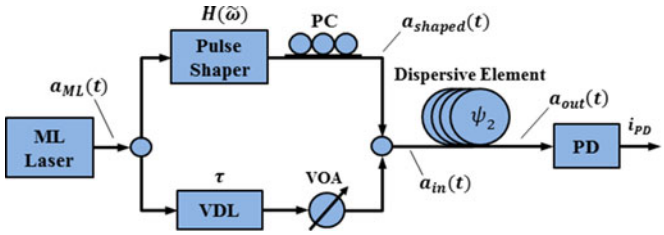

Fig. 1. Basic system configuration schematic.

One main weakness of current photonic RF-AWG technology is the baseband nature of these techniques, which creates some implications in terms of TBWP. Although recent advances have demonstrated an impressive ability to generate arbitrary waveforms spanning DC to 41 GHz with a TBWP of ~280 [22], in high-frequency passband scenarios, these schemes tend to fall quite short of their maximum achievable performance characteristics. Also, as will be discussed later, even in baseband settings, the maximum achievable TBWP values are only half of the capability provided by the photonic infrastructure, i.e., the number of resolvable optical pulse shaper resolution elements [22].

In this paper, we present a novel scheme for photonic generation of arbitrary microwave and MMW pulses based on optical interferometry, pulse shaping and frequency-to-time mapping. Our interferometric shaping design easily enables independent control over the arbitrary center frequency, temporal amplitude and temporal phase of the generated waveform. We also verify the ability to successfully achieve the upper-bound time-bandwidth product capability from our setup, regardless of the center frequency of the desired waveform. In-depth theoretical analysis and numerical simulations are accompanied by experimental results for two favorable classes of waveforms; namely ultra-wideband continuous frequency-chirped pulses and wideband frequency-hopped spread spectrum sequences.

II. Theoretical Analysis

The basic schematic of our proposed technique is depicted in Fig. 1. The system consists of a short-pulse mode-locked (ML) laser, an interferometric pulse shaping subsystem, a quadratic dispersive element, and a high speed photodetector (PD). The interferometric shaping subsystem is composed of an optical pulse shaper and a polarization controller (PC) in one arm; as well as a variable delay line (VDL) and a variable optical attenuator (VOA) in the other. In Fig. 1, $a_{\mathrm{ML}}(t)$ denotes the complex temporal envelope function of the short optical pulses created within the ML laser cavity. For the sake of theoretical analysis, we assume a flat optical spectrum for these pulses spanning an optical bandwidth of B about the center frequency ω_0 in radians per second. Thus, the Fourier representation of the ML pulses is expressed as $A_{\mathrm{ML}}(\tilde{\omega})$. Note that we use the symbol $\tilde{\omega} = \omega - \omega_0$ for frequency in rad/s to emphasize that $A_{\mathrm{ML}}(\tilde{\omega})$ is a the complex spectral envelope function corresponding to $a_{\mathrm{ML}}(t)$.

Upon arrival at the optical interferometer, the wideband pulses from the ML laser are equally split into two arms using a 50–50 optical splitter. The high-resolution pulse shaper then imparts a programmable transfer function (independently in amplitude and phase) onto the pulses travelling across the top arm; while the other arm merely delays the signals that traverse through it. The PC and VOA are employed in the general design only to ensure perfect matching of the polarization state and optical power of the pulses travelling through the two interfering arms. Therefore, without any loss of generality we can neglect these components' effects in mathematical evaluations.

According to the above explanations, we can express the Fourier transform of the signals in Fig. 1 as

$$A_{\mathrm{shaped}}(\tilde{\omega}) \propto A_{\mathrm{ML}}(\tilde{\omega}) \cdot H(\tilde{\omega}) \tag{1a}$$

$$A_{\mathrm{in}}(\tilde{\omega}) \propto A_{\mathrm{shaped}}(\tilde{\omega}) + A_{\mathrm{ML}}(\tilde{\omega}) \cdot e^{-j\omega\tau} \propto \left(H(\tilde{\omega}) + e^{-j(\tilde{\omega}+\omega_0)\tau}\right) \tag{1b}$$

where τ is the delay applied using VDL and $H(\tilde{\omega})$ is the shaper's programmable transfer function. To be completely general, we must keep in mind that $\tilde{\omega} \in [-B/2, B/2]$.

At this point, the spectrum of the optical waveform has been appropriately shaped via the programmable interferometric shaper, resulting in a field which we denote by its complex envelope $a_{\mathrm{in}}(t)$. In order to map this arbitrariness to the time domain, frequency-to-time mapping (FTM) can be effectively utilized. FTM is implemented via the introduction of a purely quadratic dispersive element subsequent to the interferometric shaping subsystem. Mathematically, the transformation of a pulse passing a medium with first-order chromatic dispersion (ψ_2) can be expressed by the Fresnel integral as follows:

$$a_{\mathrm{out}}(t) \propto e^{-j\left(\frac{t^2}{2\psi_2}\right)} \int_{\sigma_{\mathrm{in}}} a_{\mathrm{in}}(t')\, e^{-j\left(\frac{t'^2}{2\psi_2}\right)} e^{j\left(\frac{tt'}{\psi_2}\right)} dt' \tag{2}$$

where the integral is computed over the time aperture σ_{in} of the signal $a_{\mathrm{in}}(t)$ to derive $a_{\mathrm{out}}(t)$ from Fig. 1.

When the amount of dispersion is sufficient such that $\sigma_{\mathrm{in}}^2/2|\psi_2| \ll \pi$, the *far-field limit* is satisfied [25], [26] and the quadratic phase factor $\exp\left(-jt'^2/2\psi_2\right)$ in the integral in (2) may be neglected. In this limit the target RF waveform's intensity is simply a scaled replica of the optical power spectrum, i.e.,

$$|a_{\mathrm{out}}(t)|^2 \propto \left|A_{\mathrm{in}}\left(\tilde{\omega} = \frac{-t}{\psi_2}\right)\right|^2 \tag{3}$$

However, satisfying the far-field condition in our setup is not as trivial as it seems, since as a result of the delay τ, the signal $a_{\mathrm{in}}(t)$ now may potentially have a larger time aperture as compared to $a_{\mathrm{shaped}}(t)$. To take into account this hidden, but critically important consideration in our calculations, we expand (2) in terms of its components, $a_{\mathrm{shaped}}(t)$ and $a_{\mathrm{ML}}(t)$, as follows

$$a_{\mathrm{out}}(t) \propto e^{-j\left(\frac{t^2}{2\psi_2}\right)} \times \left\{ \int a_{\mathrm{shaped}}(t')\, e^{-j\left(\frac{t'^2}{2\psi_2}\right)} e^{j\left(\frac{tt'}{\psi_2}\right)} dt' + \int a_{\mathrm{ML}}(t'-\tau)\, e^{-j\left(\frac{t'^2}{2\psi_2}\right)} e^{j\left(\frac{tt'}{\psi_2}\right)} dt' \right\} \tag{4}$$

Through (4), one can see that by choosing ψ_2 large enough to satisfy the far-field limit for $a_{\rm shaped}\,(t)$, the quadratic phase term is eliminated only from the first integral; whereas the requirement for the second integral appears to be more demanding and apparently dependent on the delay variable, τ. With a change of variables and after reorganizing the phase terms, we can express the second integral in (4) as

$$\int a_{\rm ML}\,(t'-\tau)\,e^{-j\left(\frac{t'^2}{2\psi_2}\right)}e^{j\left(\frac{tt'}{\psi_2}\right)}dt' = e^{-j\left(\frac{\tau^2}{2\psi_2}\right)}e^{j\left(\frac{t\tau}{\psi_2}\right)}\int_{\sigma_{\rm ML}} a_{\rm ML}\,(t')\,e^{j\frac{tt'}{\psi_2}}e^{-j\frac{(t'+2\tau)t'}{2\psi_2}}dt' \quad (5)$$

where $\sigma_{\rm ML}$ is the time aperture of the extremely short optical pulses, which is on the order of a hundred femtoseconds in our experiments. Using a similar argument to that of the far-field condition [25], [26], the last phase term in the integral in (5) can be ignored assuming that

$$\left|\frac{\sigma_{\rm ML}\,(2\tau+\sigma_{\rm ML})}{2\,|\psi_2|}\right| \simeq \left|\frac{\tau\sigma_{\rm ML}}{\psi_2}\right| \ll \pi \quad (6)$$

Later, through our numerical and experimental results, we show that for generating waveforms in the MMW, microwave and sub-THz regions, τ is required to take on values from a few tens to hundreds of picoseconds and more, which justifies the approximation $|\tau| \gg \sigma_{\rm ML} \simeq 0.1$ ps in (6).

Assuming (6) is satisfied, the last phase term in the integral in (5) is negligible, and we have

$$\int_{a_{\rm ML}} (t'-\tau)\,e^{-j\left(\frac{t'^2}{2\psi_2}\right)}e^{j\left(\frac{tt'}{\psi_2}\right)}dt' \simeq e^{-j\left(\frac{\tau^2}{2\psi_2}\right)}e^{j\left(\frac{t\tau}{\psi_2}\right)}\int_{\sigma_{\rm ML}} a_{\rm ML}\,(t')\,e^{j\frac{tt'}{\psi_2}}dt' = e^{-j\left(\frac{\tau^2}{2\psi_2}\right)}.e^{j\left(\frac{t\tau}{\psi_2}\right)}.A_{\rm ML}\left(\tilde{\omega}=\frac{-t}{\psi_2}\right) \quad (7)$$

From (4) and (7), when both the far-field condition for $a_{\rm shaped}\,(t)$ and the requirement in (6) are fulfilled, we have

$$|a_{\rm out}\,(t)|^2 \propto \left|A_{\rm shaped}\left(\tilde{\omega}=\frac{-t}{\psi_2}\right)+e^{-j\left(\frac{\tau^2}{2\psi_2}\right)}.e^{j\left(\frac{t\tau}{\psi_2}\right)}.A_{\rm ML}\left(\tilde{\omega}=\frac{-t}{\psi_2}\right)\right|^2 \quad (8)$$

We prove later in this section that the constraint in (6) is independent of, and thus not contradictory to, the far field condition for $a_{\rm shaped}\,(t)$, and is always satisfied for waveforms up to the sub-THz frequency regime.

With these assumptions in mind, by substituting (1a) in (8), the following equation describes the photodetected current.

$$i_{\rm PD}\,(t) \propto |a_{\rm out}\,(t)|^2 \propto 1+\left|H\left(\frac{-t}{\psi_2}\right)\right|^2 + 2\left|H\left(\frac{-t}{\psi_2}\right)\right|.\cos\left(\frac{t\tau}{\psi_2}-\angle H\left(\frac{-t}{\psi_2}\right)+\phi_0\right) \quad (9)$$

where $\phi_0 = -\tau^2/2\psi_2$ is just a constant phase term.

Note that in (9), we have dropped the $|A_{\rm ML}\,(\tilde{\omega})|$ terms, owing to the fact that the original spectrum is flat and frequency independent. Also, $H\,(\tilde{\omega})$ is decomposed into its independent phase and amplitude terms using the corresponding symbols.

The current flowing through the PD can be decomposed into two individual terms; a positive baseband component, namely $1+|H(\frac{-t}{\psi_2})|^2$, and a programmable passband component described as

$$i_{\rm des}\,(t) \propto \left|H\left(\frac{-t}{\psi_2}\right)\right|.\cos\left(\frac{t\tau}{\psi_2}-\angle H\left(\frac{-t}{\psi_2}\right)+\phi_0\right) \quad (10)$$

The shorthand notation $i_{\rm des}\,(t)$ is employed to emphasize that this component of the PD current is the *desired* signal and will be the main focus of this paper hereon in.

Equation (10) demonstrates the ability of the proposed scheme to independently control the temporal amplitude, temporal phase and center frequency of $i_{\rm des}\,(t)$ through the pulse shaper amplitude, pulse shaper phase and the applied delay using VDL, respectively. To be more specific, we have

$$\text{Temporal Amplitude} \propto \left|H\left(\frac{-t}{\psi_2}\right)\right| \quad (11a)$$

$$\text{Temporal Phase} = \frac{t\tau}{\psi_2}-\angle H\left(\frac{-t}{\psi_2}\right)+\phi_0\ \text{rad} \quad (11b)$$

$$\text{Center Frequency} = f_c = \left|\frac{\tau}{2\pi\psi_2}\right|\ \text{Hz} \quad (11c)$$

The above three equations clearly show the simplicity of the described RF-arbitrary waveform generation (RF-AWG) method. At the far-field limit, for a fixed value of dispersion, setting the appropriate value for τ enables extremely wide-range center frequency tuning, while manipulating the phase and amplitude function of the pulse shaper enables independent control over the arbitrary amplitude and phase function of the generated signal.

At this point we are also able to present a clear proof regarding the satisfaction of (6). According to (11c), we can express τ in terms of the desired center frequency (f_c) and the dispersion amount (ψ_2). This can be substituted in (6) and after some cancellations, the statement is changed to

$$2f_c\sigma_{\rm ML} \ll 1 \quad (12)$$

It is clear from (12) that this requirement is independent of ψ_2 and is only governed by f_c. As a result, this constraint and the far-field condition can be simultaneously satisfied. Also, for $\sigma_{\rm ML} \simeq 0.1$ ps, center frequency values up to 500 GHz are still within the boundaries of (12), facilitating access to high-fidelity μ-wave, MMW and sub-THz RF-AWG territory.

Moreover, this is the first design to our knowledge that successfully engineers programmable RF waveforms with time-bandwidth products equal to the upper bound given by the number of spectrally resolved pulse shaper control elements ("*resolution elements*" in the following). This is a direct result of creating the center frequency fringes of the desired signal using optical interferometry, which liberates the pulse shaper to devote all of its resolution elements solely to passband modulation features.

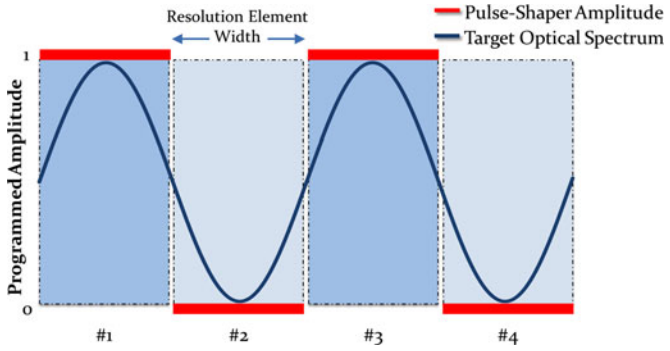

Fig. 2. Cartoon representation of pulse shaper resolution elements for generating the fastest possible oscillations using conventional (baseband) FTM-based RF-AWG.

As we now briefly explain, this is in contrast to conventional FTM-based RF-AWG schemes [12]–[15], [22], which are limited to time-bandwidth products equal to only half of this value. Conventional schemes are inherently baseband, meaning that the maximum achievable bandwidth (and hence TBWP) is equal to the fastest frequency oscillations that can be generated using these schemes. Since these techniques are based on amplitude-only spectral shaping, to create the fastest possible sinusoidal cycle, one must consume at least two pulse shaper resolution elements (one for the positive half-cycle and one for the negative half-cycle). A simple depiction of this is provided in Fig. 2, showing the target optical spectrum and corresponding function programmed onto the pulse shaper. As a result, after FTM, the maximum achievable frequency, $f_{\max}$ in Hz, is

$$f_{\max} \simeq \frac{1}{2\delta\omega \times |\psi_2|} \tag{13}$$

where $\delta\omega$ denotes the frequency sweep across the width of one pulse shaper resolution element in rad/s.

Also, the RF waveform's temporal duration, ΔT_{RF}, is

$$\Delta T_{\mathrm{RF}} = B \times |\psi_2| = N\delta\omega \times |\psi_2| \tag{14}$$

where B is the pulse shaper operational bandwidth and N is the total number of resolution elements. Equations (13) and (14) give the TBWP of conventional FTM-based RF-AWG as

$$\mathrm{TBWP} = \Delta T_{\mathrm{RF}} \times \mathrm{BW}_{\mathrm{RF}} \simeq \Delta T_{\mathrm{RF}} \times f_{\max} = \frac{N}{2} \tag{15}$$

where $\mathrm{BW}_{\mathrm{RF}}$ is the RF bandwidth of the generated pulse.

Thus, (15) clearly shows that for baseband RF-AWG schemes, the TBWP is capped at half the number of pulse shaper resolution elements, and one cannot use the full N degrees of freedom provided by the pulse shaper. In the next sections, we show that our proposed interferometric RF-AWG scheme can actually achieve TBWP values in the proximity of this limit (N), which can be considered as an upper-bound for all photonic-assisted RF arbitrary waveform generation.

III. Numerical Simulation

In order to accompany the mathematical evaluations, appropriate numerical analysis, incorporating the Fresnel integral, is presented in this section. Here, the main concentration is directed toward two classes of interesting waveforms: specifically ultra-wideband continuous frequency- chirped electrical pulses; as well as wideband frequency- hopped spread spectrum (FHSS) sequences. To match our experimental apparatus, we have assumed that the ML laser covers the full optical C-band (5 THz bandwidth); the pulse-shaper also spans the C-band with 10 GHz spectral resolution and 1 GHz addressability; and ~25 km of single-mode fiber (SMF) acts as the quadratic dispersive element with dispersion value 393.6 ps/nm (i.e., $\psi_2 = -501.67$ ps^2).

Note that here we distinguish between resolution and addressability: addressability refers to the frequency sweep across individual spatial light modulator pixels, whereas resolution refers to the minimum feature size that can be imprinted onto the output spectrum, limited by the finite optical spot size at the spatial light modulator plane. In all simulations, the smooth phase and amplitude functions are represented as stair-step waveforms with 1 GHz steps (matching the 1 GHz addressability of the physical device); these are then convolved with a 10 GHz Gaussian to account for the finite spectral resolution, using eq. (8.34) from [27].

A. Ultra-Wideband Continuous Frequency-Chirps

Generating microwave and millimeter wave continuous frequency-chirped pulses is desirable for high-resolution radar and sensing systems as well as other applications like biomedical imaging and physical chemistry [1]–[4]. Chirped pulses not only have the advantage of high temporal resolution similar to ultrashort electrical pulses, but they also avoid many design issues like saturation and amplifier nonlinearity at the transmitter end. This is why the generation of this class of waveforms, specifically ultra-wideband linear frequency-chirps, has been an attractive research topic for various groups working on signal design [16]–[19].

In the first simulation, we study the generation of an ultra-wideband linear frequency-chirped pulse across a desired center frequency using our introduced technique. We aim to attain signals with the best possible compression ratio (i.e., the most compressed autocorrelation), which is directly proportional to the TBWP criterion of the generated waveform. Fig. 3 shows the temporal and spectral representations for a simulated example. The delay variable is set to $\tau = 189$ ps to realize a center frequency of $f_c = 60$ GHz, while a spectral phase function of $\angle H(\tilde{\omega}) = 2e^{-24}\tilde{\omega}^2$ rad is programmed onto the pulse shaper.

The instantaneous frequency information in Fig. 3(a) is defined based on the following definition

$$f_{\mathrm{inst}}(t) = \frac{1}{2\pi}\frac{d}{dt}\phi_{\mathrm{RF}}(t) \tag{16}$$

where $\phi_{\mathrm{RF}}(t)$ is the temporal phase function of the generated RF waveform, corresponding to (11b) in radians and $f_{\mathrm{inst}}(t)$ has units of inverse seconds (or Hz). It is clear from the instantaneous frequency plot of Fig. 3(a) that the generated signal is a smooth constant-amplitude linear downchirp. This matches perfectly with our expectations, since from (11b) the temporal frequency

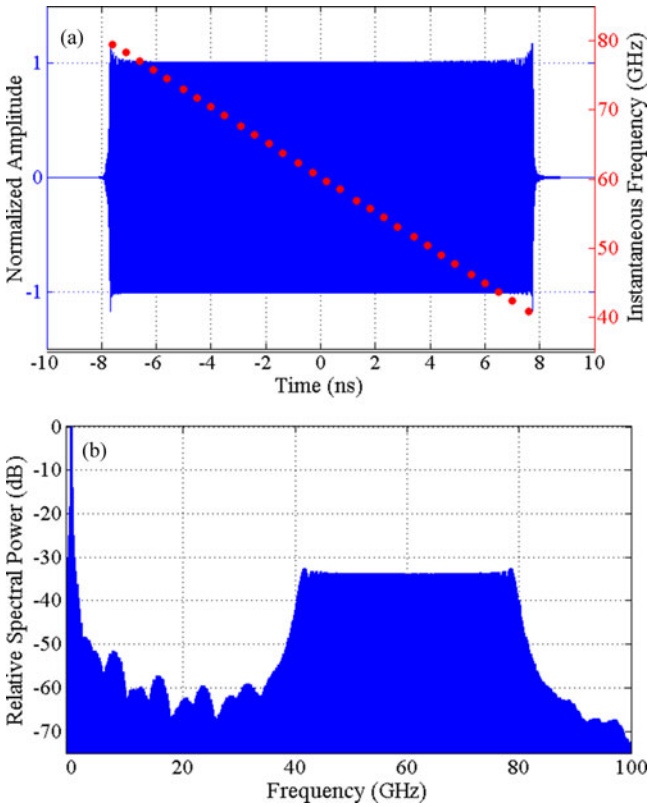

Fig. 3. Ultra-wideband linear frequency downchirp simulation result. (a) DC-blocked temporal waveform i_{des} and instantaneous frequency. (b) Power spectrum of photodetected waveform i_{PD}.

of the desired waveform is proportional to the derivative of the applied pulse shaper phase function.

It is necessary to note that the applied phase function is constrained by the finite spectral resolution, as explained in [27]. The finite spectral resolution results in a phase-to-amplitude conversion effect, which introduces an attenuation that becomes important when the spectral phase varies too rapidly (hence when the target RF frequency offset becomes too large). In the simulation reported here, we chose a quadratic phase function resulting in a maximum phase jump of $\pi/8$ for adjacent 1 GHz-spaced addressable pixels, corresponding to $5\pi/4$ variation per 10 GHz resolution element. This value matches that used in our experiment reported below in Section IV and is selected based on the amount of amplitude attenuation we could practically tolerate and still be able to flatten out (equalize) the spectrum and then amplify back to adequate power levels at acceptable signal-to-noise. The equalization step is performed using the same pulse shaper by taking advantage of its programmable amplitude, which (aside from spectral resolution constraints) can be programmed independently of phase. In simulating this equalization, the shaper addressability and resolution are accounted for in the same way as described before.

From Fig. 3, the resultant photodetected signal has a time duration of 15.75 ns and a 3 dB bandwidth of 38 GHz, making the TBWP of the simulated linear frequency-chirped pulse 598.5. This value is, as expected, in the proximity of the maximum achievable TBWP using the aforementioned pulse shaper resolution (5 THz bandwidth divided by 10 GHz resolution yields 500 resolvable elements). The precise value of achievable TBWP depends on the amount of phase-to-amplitude conversion one is willing to accept in the experimental implementation.

TABLE I
LENGTH 15 COSTAS SEQUENCE

Frequency Hop Sequence Ordering
4, −3, 3, −5, −4, 0*, −2, −6, 1, 6, 5, 7, 2, −1, −7

*Zero denotes no frequency shift.

These simulation results support our claim that the proposed interferometric scheme should provide TBWP twice that of what can be realized using conventional FTM methods [12]–[15]. The interferometric scheme provides further advantage for passband signals. This is due to the fact that, as elaborated in the previous section, for conventional, baseband FTM-based RF-AWG, the maximum TBWP is only achieved for a signal spanning from dc to the highest frequency generated. So, if one aims to generate a passband signal, quite a lot of TBWP will be sacrificed. To be more clear, in the case of the target signal spanning from 41 to 79 GHz (the result of our simulation in Fig. 3), the maximum TBWP that baseband FTM methods can achieve is roughly

$$\frac{500}{2} \times \frac{38\ \mathrm{GHz}}{79\ \mathrm{GHz}} \simeq 120.25 \tag{17}$$

Therefore, in this specific example our proposed method achieves nearly 5 times more TBWP in comparison with baseband FTM-based RF-AWG schemes, including near field frequency-to-time mapping [22].

B. Wideband Frequency-Hopped Spread Spectrum Sequence

Another very interesting set of waveforms with applications in radar engineering, imaging and communications are FHSS sequences. A criterion often used for evaluating the compression performance of FHSS sequences is the auto-ambiguity function [28]. This function not only measures the compression of a pulse in the time domain (corresponding to range), but also in frequency (corresponding to Doppler). The advantage of wideband implementation of these signals using our technique is that we allow the user to effortlessly design the range and velocity resolution within a wide span of values without any significant setup modification.

In this work we have chosen an FHSS sequence from a family of sequences proven to have optimal (thumbtack) auto-ambiguity compression. These frequency-coded signals are called Costas sequences and have a broad extent of applications in high-resolution ranging, detection and synchronization [28], [29]. Here, a Costas sequence of length 15 and fundamental frequency of 1 GHz is created about a 30 GHz carrier frequency. This corresponds to programming a piecewise linear phase on the pulse shaper and setting τ equal to 94.5 ps. The harmonic ordering for this sequence is tabulated in Table I.

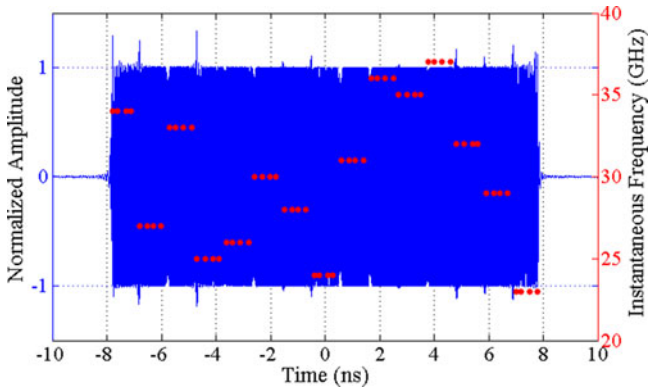

Fig. 4. Wideband Costas sequence simulation result - dc-blocked temporal waveform i_{des} and instantaneous frequency.

Fig. 4 illustrates the Costas sequence simulation results. Clear transitions in temporal frequency are observed about the 30 GHz frequency range. A practically flat amplitude is also visible for this signal, although it should be noted that the slight amplitude overshoots at the transitions are due to the finite resolution of the pulse shaper, which has been taken into account in all simulations.

IV. Experiments and Results

In order to realize our proposed scheme experimentally, the system configuration should be enhanced to incorporate issues like power handling, stabilization, polarization matching, dispersion compensation, and noise reduction. Fig. 5 shows the resultant detailed experimental setup. The signal generation path is illustrated from left to right, starting at an erbium-doped fiber ring mode-locked laser and ending at a high-speed photodetector. The ML laser has a repetition rate of ~53 MHz and spans 1520 to 1610 nm. In order to match the bandwidth to that of the pulse shaper, we added a home-made optical bandpass filter to sift out only the C-band (5 THz optical bandwidth) from the mode-locked laser output and flatten out the optical spectrum. An erbium-doped fiber amplifier and a PC follow before pulses enter the interferometric shaping subsystem.

The interferometric shaping subsystem is composed of polarization maintaining (PM) components so as to prevent polarization drift and eliminate the need for polarization matching. A commercial PM pulse shaper (Finisar 1000SP) with spectral resolution of ~10 GHz spanning the full optical C-band operates as the means for arbitrary waveform generation. Also, for stability purposes, a piezo-electric transducer (PZT) is implanted within the interferometer to act as an actively controllable fiber stretcher. The output pulses from the interferometric shaping subsystem are stretched in ~25 km of SMF (total dispersion of ~393.6 ps/nm) and amplified again before beating on a high-speed 50 GHz photodetector. All measurements are made using a 70 GHz digital sampling oscilloscope with 50 Ω input impedance.

The interferometer stabilization path flows from right to left inside the same configuration (shown beneath the generation path in Fig. 5). Details of the stabilization procedure and its components are explained in the next section.

A. Experimental Setup Stabilization

Regardless of the application, an optical interferometer requires modifications in order to enhance its stability against vibrations and relative temperature fluctuations between the two arms. It is usually important to maintain a constant phase difference between the two interfering arms. From our point of view, the main drawback of an unstable phase difference inside the interferometer is the repeatability of the generated waveforms. For instance, in spread spectrum settings, the compressibility of a series of wideband chirped signals is of great importance. This can be achieved using real-time or offline auto- and cross correlation [28], [29]. If the created waveforms are consistently repeatable, pulse compression can be implemented using only one stored copy of the sequence. However, in the presence of an unstable phase difference, either phase tracking must be implemented via digital signal processing or every single sequence element must be recorded, substantially increasing system complexity.

To simply show this effect, we conducted an experiment on our unstabilized setup. Over the period of 2 hours, we took 750 different measurement samples of the same linear frequency-chirped waveform programmed using the proposed technique. All of these waveforms span approximately 16 ns in time and 10–30 GHz in frequency. Fig. 6 shows the result of the overlaid cross correlations between 4 different samples and a chosen reference from this measurement batch. The solid blue curve plots the reference sample's autocorrelation (illustrating compression from 16 ns to less than 0.1 ns), while the other 3 plots correspond to the various cross correlations. In theory, it is expected that phase fluctuations between the two arms of our interferometer translate into drift in the relative temporal phase between each sample chirp. From the cross-correlation point of view, this would lead to correlation peak displacement, attenuation, distortion, and even flipped polarity, all of which are observable from Fig. 6. It should be noted that although all of the cross-correlation plots in Fig. 6 depict signal compression from the original ~16 to ~0.1 ns, the fact that the correlation plots are not matching introduces significant complications for most applications.

In order to overcome issues arising due to unstable phase fluctuations, we resort to a simple feedback stabilization technique [30]. As depicted in Fig. 5, an independent CW optical wave, followed by a PC, is fed into the interferometer from the opposite direction as a probing signal. By taking the opposite propagation direction, we have effectively allow frequency overlap between our CW signal and the mode-locked spectrum; while at the same time avoiding the need for extra optical filtering. The CW signal travels through the interferometer from right to left and after coupling out of the 2×2 50-50 coupler impinges on an ordinary photodetector. The bandwidth of this PD is ~1 GHz, which is more than adequate for detecting the slowly varying phase fluctuations in our setup, which if not compensated alter the photodetected intensity.

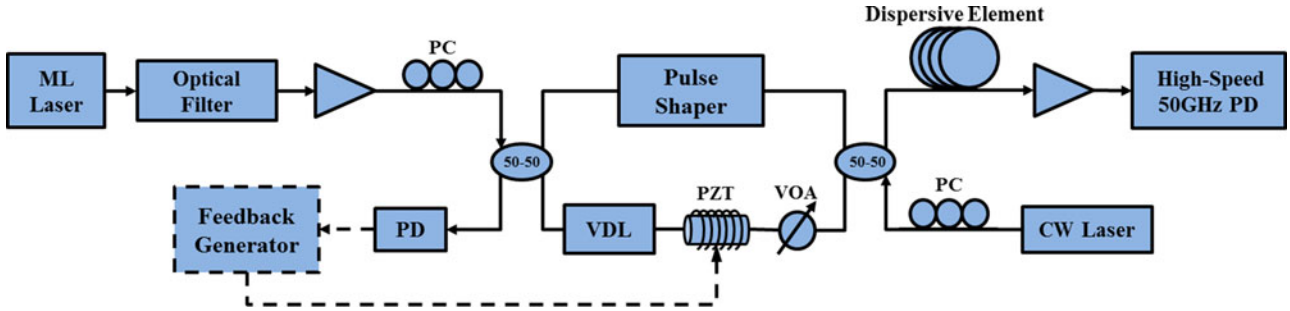

Fig. 5. Detailed experimental setup.

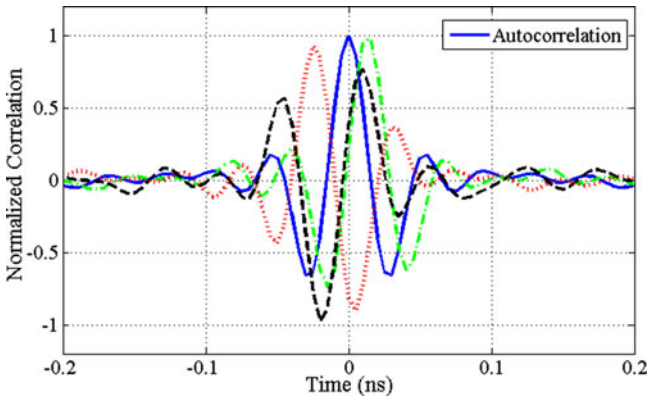

Fig. 6. Cross-correlation plots of four sample linear chirps created in the unstabilized setup with respect to a common reference.

Using appropriate electrical feedback components and the piezo-electric fiber stretcher (PZT), we lock this intensity to a constant value and thus accomplish interferometer stability. With this improvement, we are able to stabilize the interferometer and achieve repeatable waveform results without RF phase drift, as shown in the following sections.

B. Ultra-Wideband Continuous Frequency-Chirp

In this section, we demonstrate waveforms similar to those simulated in Section III-A, but reduced to $f_c = 25$ GHz (corresponding to a delay of roughly 78.75 ps) in view of the frequency response of our photodetector. In order to create the linear chirping function, we apply the same phase-only function on the pulse shaper, i.e., $\angle H\,(\tilde{\omega}) = 2e^{-24}\tilde{\omega}^2$

Fig. 7 displays the temporal and spectral results for this experiment. The dc-blocked signal - denoted by $i_{\rm des}$ in our analytical evaluations - is depicted in Fig. 7(a) alongside its instantaneous frequency plot; while Fig. 7(b) shows the corresponding power spectrum of the total photodetected waveform. In addition to phase shaping, the pulse shaper is used to equalize the effect of phase-to-amplitude conversion, explained earlier, as well as spectral ripple present on the input laser and optical amplifier nonuniformities across the spectrum. As a result the very flat temporal amplitude observed in Fig. 7(a) is obtained. Such spectral amplitude control can be further exploited for implementing applications like windowing and sidelobe suppression [28].

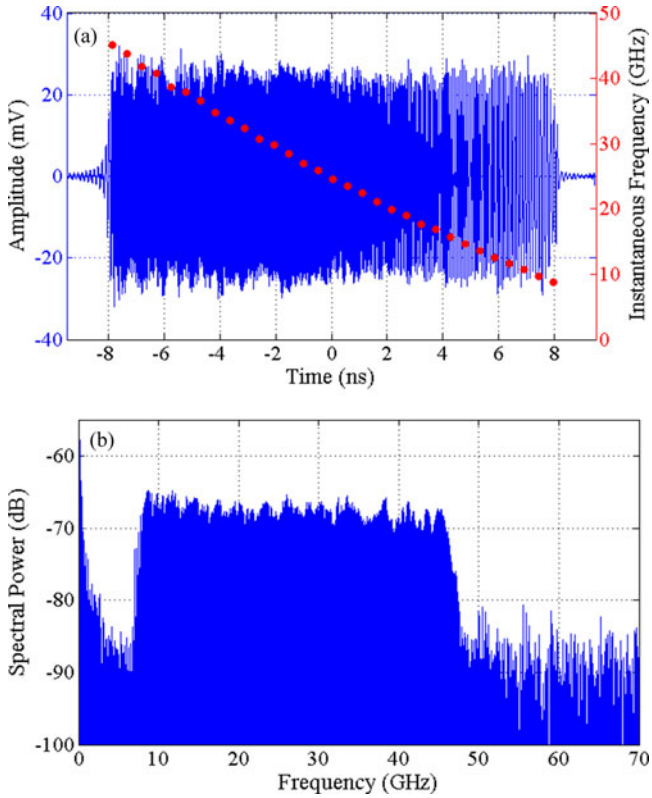

Fig. 7. Ultra-wideband linear frequency downchirp experimental result. (a) DC-blocked temporal waveform $i_{\rm des}$ and instantaneous frequency. (b) Power spectrum of photodetected waveform $i_{\rm PD}$.

We remark that, the slight curve in the instantaneous frequency in Fig. 7(a) is due to higher-order dispersion (mainly second) in the 25 km SMF and agrees with dispersion specifications of the fiber and experimental parameters published in [31]. We show in the next section that our scheme can also allow us to compensate for this undesirable higher-order dispersion and achieve a truly-linear downchirp.

From Fig. 7, the demonstrated waveform has a pulse duration of ~15.75 ns and a 3-dB bandwidth of ~37.4 GHz, yielding a total TBWP of ~589. As anticipated, this number is in the vicinity of the number of programmable spectral resolution elements on the aforementioned pulse-shaper.

Next, we show the repeatability of these engineered waveforms. In order to do so, 750 samples of the generated waveform

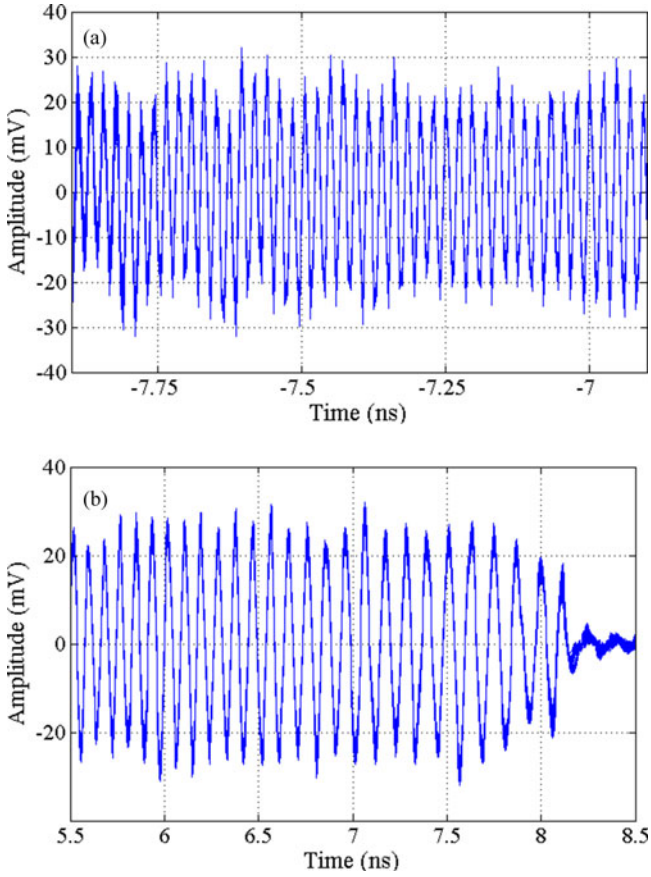

Fig. 8. Overlaid temporal representation of 750 different sample measurements of the ultra-wideband linear frequency downchirp in Fig. 7 Zoomed-in views at (a) higher frequency region (b) lower frequency region.

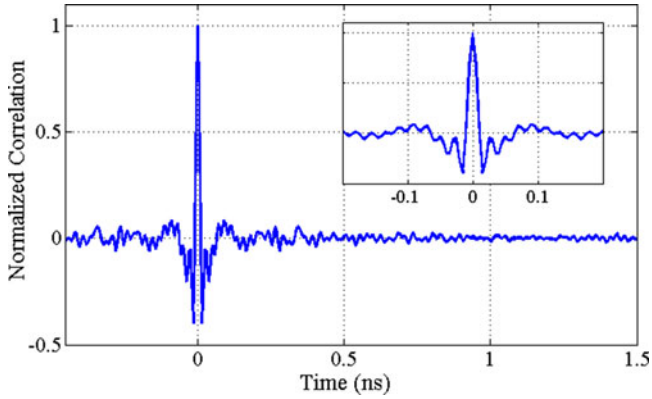

Fig. 9. Overlaid cross-correlation plots of 750 different sample measurements of the ultra-wideband linear frequency downchirp in Fig. 7 with respect to a common reference.

in Fig. 7 were taken once every 10 seconds over the time period of approximately 2 hours. Fig. 8 displays the overlay of all the different samples from this batch. The waveforms are so closely similar that no distinction is apparent in a full scale view. Thus, Figs. 8(a) and 7(b) each show a zoomed-in view at the higher and lower frequency parts of these signals. Clearly, there are only very minor temporal distinctions between various sample waveforms. This leads to an average correlation coefficient [32] of 99.31% over all the 750 sample signals, while without stabilization, the correlation is extremely low due to the effects of RF phase drift.

From the cross-correlation perspective, this repeatability is even more evident since it shows that the still-existing minute temporal dissimilarities between different sample waveforms have insignificant effect when it comes to the compressibility of the different signals. Fig. 9 contains cross-correlation plots of all 750 waveforms with respect to a common reference. It is evident from the indistinguishable curves in this figure that all 750 signals have been successfully compressed from ~16 ns to less than 30 ps and all correlation plots match the autocorrelation of a single waveform very well. In other words, no distinct sign of cross-correlation distortion, peak displacement, attenuation or flipped polarity is witnessed.

We conclude this section by briefly comparing with examples of previous research in programmable chirp generation. References [17], [18], which are also based on FTM, demonstrate control over the center frequency and, to a certain extent, the chirp-rate of linear frequency-chirped MMW pulses, but exhibit TBWPs below 50. Another approach, based on beating a rapidly tuned laser diode with a fixed frequency laser, provides extremely high TBWP values for linear/nonlinear chirp generation [19]. However, because the frequency sweep of the laser diode is not exactly repeatable, the repeatability of the generated chirp waveforms is compromised. Finally, we note that all the aforem entioned techniques are aimed at chirped waveform generation and are not capable of RF arbitrary waveform generation.

C. Higher-Order Dispersion Compensation

In the previous section we presented clear results regarding repeatable frequency-chirped waveforms with large TBWP values. However, as observed from Fig. 7(a), these chirps were not truly linear and did not agree 100% with our numerical analysis. This is apparent in the slight curve in the instantaneous frequency plot of Fig. 7(a). The main reason for this phenomenon is the existence of higher order dispersion in our experimental dispersive element block. In this section we show the capability of our proposed RF-AWG configuration to compensate these unwanted higher-order dispersion effects and experimentally achieve truly linear frequency-chirps.

As we discussed in our theoretical analysis, perfect frequency-to-time mapping requires the use of a purely first order (quadratic phase) dispersive element. Nevertheless, since we are utilizing regular SMF for FTM, it is also expected that one observes the effect of a certain amount of higher order dispersion. Based on the specifications of the utilized fiber spool as well as previous experimental analysis in our group on the same fiber [31], we expect this higher order dispersive effect to be dominated by second order (cubic phase) dispersion.

Fig. 10(a) shows the spectrogram plot of a sample waveform generated from our setup without dispersion compensation, us-

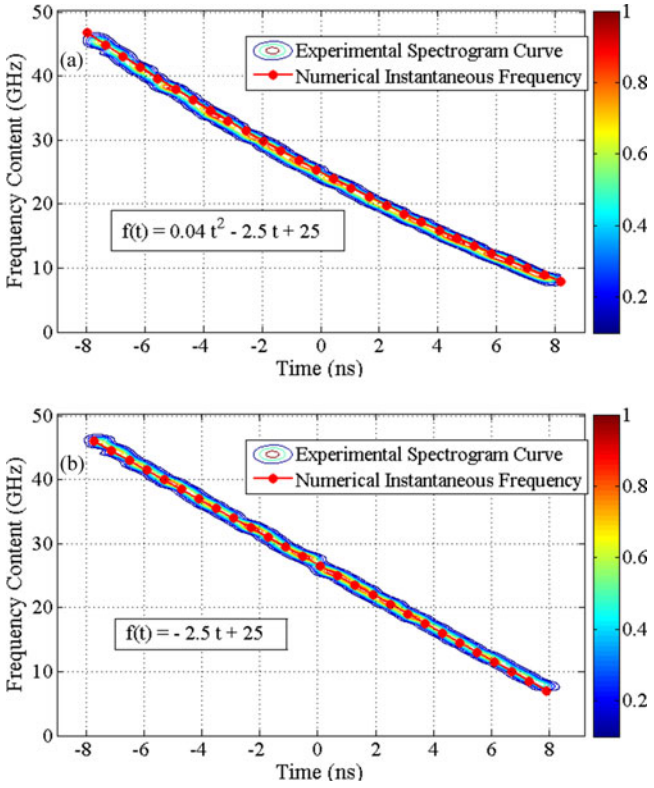

Fig. 10. Experimental spectrogram curve and numerical instantaneous frequency of (a) uncompensated linear frequency chirp (b) dispersion compensated *truly-linear* frequency chirp.

ing the following definition of spectrogram [27]

$$S_e(f,\tau) = \left| \int_{\mathrm{PD}}^{i} (t)\, g(t-\tau)\, e^{-j2\pi f t} dt \right|^2 \qquad (18)$$

where the gate function, $g(t)$, was chosen to be a Gaussian pulse with 500 ps pulse duration.

Ideally, in the presence of purely first order dispersion, the waveform is expected to exhibit precise linear frequency chirping behavior. The slightly arched chirping function of this waveform can be numerically calculated using the dispersion slope parameter (only cubic spectral phase) of the SMF spool. This expected instantaneous frequency curve is plotted on top of the spectrogram, accompanied by its time-varying instantaneous frequency function (time in ns and frequency in GHz). The extreme resemblance of these two curves verifies that, in agreement with our prior anticipations, the undesirable higher order dispersion of our fiber spool is dominated by second order dispersion.

Fig. 10(b) shows the result of compensating for the second order dispersion of the SMF spool as well as the numerical results for instantaneous frequency. In order to accomplish this dispersion compensation, an extra cubic phase was programmed onto the pulse-shaper arm of our setup. This cubic phase was chosen to exactly complement the cubic spectral phase due to the second order dispersion of the SMF and ensure accurate FTM after passing through. From Fig. 10(b), one can observe

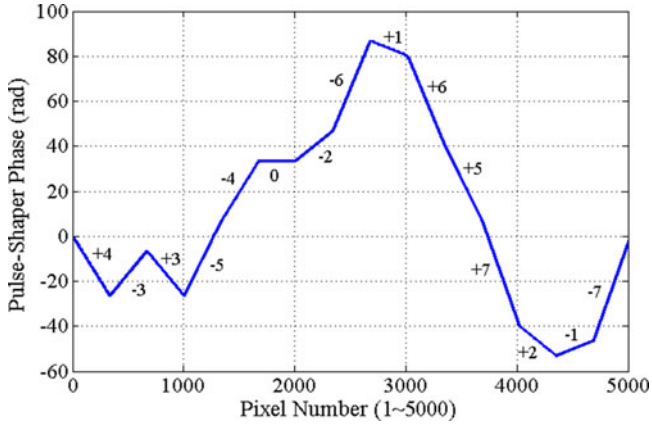

Fig. 11. Applied unwrapped phase for Costas experiment and corresponding frequency harmonics (actual phase applied to pulse shaper is modulo 2π).

that the quadratic temporal frequency term has been entirely eliminated within the precision of our measurement. Moreover, it should be noted that our compensation scheme is not limited to residual cubic phase; our configuration allows compensation of any higher order residual spectral phase function within the spectral resolution limits of the pulse shaper.

D. Wideband Frequency-Hopped Spread Spectrum Sequence

In this experiment we show the possibility of utilizing the proposed RF-AWG technique to generate Costas sequences. Here, we specifically implement the length 15 Costas sequence described in Section III-B and Table I.

In this test, the carrier frequency is set at $f_c = 10$ GHz to emphasize the tunability of the delay parameter in our setup and allow better visualization of the results; while the fundamental frequency of the sequence is 1 GHz to match the results from simulation. In order to realize this sequence, we apply a piecewise linear phase function onto the pulse shaper, where the slope of each section is proportional to each specific harmonic of the Costas array. Of course, as mentioned in the previous section, some minor phase compensation is necessary to precompensate higher-order dispersion effects.

Fig. 11 shows the corresponding unwrapped phase function applied to the pulse-shaper. It can be recognized from this figure, that at larger harmonic deviations, larger slope values must be implemented. Due to the finite pulse shaper resolution, this creates slight attenuation at high harmonics as a result of the phase-to-amplitude conversion effect [27]. These slight attenuations at high frequency deviations can be compensated for by applying some attenuation (no more than 2 dB) at other optical frequency regions using the amplitude function of the same pulse shaper.

Fig. 12 shows the generated 16 ns-long waveform for this experiment. In Fig. 12(a), the sequence is overlaid with its instantaneous frequency plot versus time. An almost smooth amplitude is distinctly visible, although as predicted, slight overshoots are present at discontinuities in the pulse shaper phase function. It

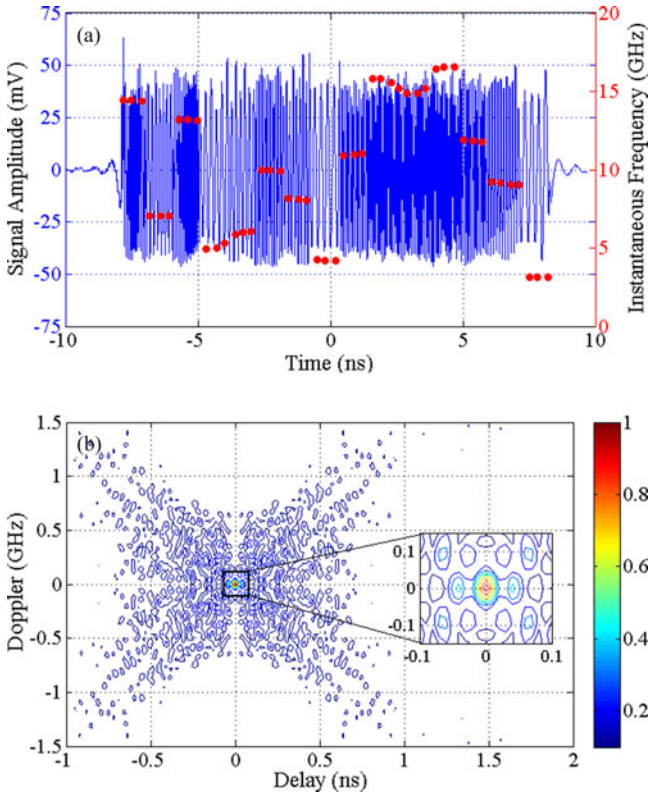

Fig. 12. Wideband Costas sequence experimental result. (a) DC-blocked temporal waveform i_{des} and instantaneous frequency. (b) Normalized contour plot of auto-ambiguity function versus delay and Doppler.

is clear that the transitions are close to what we expect; spaced out evenly in time and frequency.

To further show the performance characteristics of the generated Costas signal, its auto-ambiguity function was calculated offline. Fig. 12(b) shows this normalized auto- ambiguity. This function resembles the nice thumbtack ambiguity that is expected from the Costas sequence. The main lobe of the autoambiguity function has a full-width half-maximum (FWHM) of ~15 ps in delay and ~36 MHz in Doppler. It must be noted that the relatrively coarse Doppler resolution is as expected due to the still small temporal duration of the signals implemented [28], [29]. As a potential for future work, this RF-AWG technique can be combined with the waveform switching scheme presented in [33] to increase the repeat-free temporal duration of the generated signals from nanoseconds to microsecond and even millisecond scale. This should enable much finer frequency resolution, potentially below the kHz level, of interest for many practical applications.

V. Conclusion

In conclusion, we have demonstrated a novel photonic radio-frequency arbitrary waveform generation scheme. By use of fine-resolution optical pulse shaping, optical interferometry, and the concept of frequency-to-time mapping, our setup enables independent control over the temporal amplitude, temporal phase and center frequency of the generated waveform. A time-bandwidth product of ~589 is experimentally realized using this setup, verifying successful achievement of the upper-bound time-bandwidth product for photonic-assisted RF-AWG schemes using the same resources. We further addressed practical issues such as waveform generation stability and repeatability as well as higher-order dispersion compensation.

Acknowledgment

The authors would like to thank Senior Research Scientist Dr. D. E. Leaird for his helpful technical assistance in the experiments. Any opinion, findings, and conclusions or recommendations expressed in this publication are those of the authors and do not necessarily reflect the views of the sponsors.

References

[1] A. W. Rihaczek, *Principles of High-Resolution Radar*. Norwood, MA, USA: Artech House, 1996.
[2] A. Y. Nashashibi, K. Sarabandi, P. Frantzis, R. D. De Roo, and F. T. Ulaby, "An ultrafast wide-band millimeter-wave (MMW) polarimetric radar for remote sensing applications," *IEEE Trans. Geosci. Remote Sensing*, vol. 40, no. 8, pp. 1777–1786, Aug. 2002.
[3] M. Miyakawa and J. Ch. Bolomey, "Microwave imaging I: microwave computed tomography," *Non-Invasive Thermometry of the Human Body*. Boca Raton, FL, USA: CRC Press, 1995, pp. 105–126.
[4] G. G. Brown, B. C. Dian, K. O. Douglass, S. M. Geyer, S. T. Shipman, and B. H. Pate, "A broadband Fourier transform microwave spectrometer based on chirped pulse excitation," *Rev. Scientific Instrum.*, vol. 79, no. 5, pp. 053103.1–053103.13, 2008.
[5] C. W. Chow, L. G. Yang, C. H. Yeh, C. B. Huang, J. W. Shi, and C. L. Pan, "10 Gb/s optical carrier distributed network with W-band (0.1 THz) short-reach wireless communication system," *J. Opt. Commun.*, vol. 285, pp. 4307–4311, 2012.
[6] A. J. Seeds and K. J. Williams, "Microwave photonics," *IEEE J. Lightw. Technol.*, vol. 24, no. 12, pp. 4628–4641, Dec. 2006.
[7] J. Capmany and D. Novak, "Microwave photonics combines two worlds," *Nature Photon.*, vol. 1, no. 6, pp. 319–330, 2007.
[8] T. Nagatsuma and Y. Kado, "Microwave photonic devices and their applications to communications and measurements," *PIERS Online*, vol. 4, no. 3, pp. 376–380, 2008.
[9] J. D. McKinney and A. M. Weiner, "Photonic synthesis of ultrabroadband arbitrary electromagnetic waveforms," in *Microwave Photonics*, C. H. Lee Ed., 2nd ed. Boca Raton, FL, USA: CRC Press, 2013, pp. 243–306.
[10] J. P. Yao, "Photonic generation of microwave arbitrary waveforms," *J. Opt. Commun.*, vol. 284, no. 15, pp. 3723–3736, 2011.
[11] T. Yilmaz, C. M. DePriest, T. Turpin, J. H. Abeles, and P. J. Delfyett, "Toward a photonic arbitrary waveform generator using modelocked external cavity semiconductor laser," *IEEE Photon. Technol. Lett.*, vol. 14, no. 11, pp. 1608–1610, Nov. 2002.
[12] J. D. McKinney, D. E. Leaird, and A. M. Weiner, "Millimeter-wave arbitrary waveform generation with a direct space-to-time pulse shaper," *Opt. Lett.*, vol. 27, no. 15, pp. 1345–1347, 2002.
[13] J. Chou, Y. Han, and B. Jalali, "Adaptive RF-photonic arbitrary waveform generator," *IEEE Photon. Technol. Lett.*, vol. 15, no. 4, pp. 581–583, Apr. 2003.
[14] I. Lin, J. D. McKinney, and A. M. Weiner, "Photonic synthesis of broadband microwave arbitrary waveforms applicable to ultra-wideband communication," *IEEE Microw. Wireless Compon. Lett.*, vol. 15, no. 4, pp. 226–228, Apr. 2005.
[15] J. D. McKinney, "Background-free arbitrary waveform generation via polarization pulse shaping," *IEEE Photon. Technol. Lett.*, vol. 22, no. 16, pp. 1193–1195, Aug. 2010.
[16] W. Chao and J. P. Yao, "Photonic generation of chirped millimeter-wave pulses based on nonlinear frequency-to-time mapping in a nonlinearly chirped fiber Bragg grating," *IEEE Trans. Microw. Theory Techn.*, vol. 56, no. 2, pp. 542–553, Feb. 2008.
[17] R. Ashrafi, Y. Park, and J. Azana, "Fiber-based photonic generation of high-frequency microwave pulses with reconfigurable linear chirp control," *IEEE Trans. Microw. Theory Tech.*, vol. 58, no. 11, pp. 3312–3319, Nov. 2010.

[18] M. Li and J. P. Yao, "Photonic generation of continuously tunable chirped microwave waveforms based on a temporal interferometer incorporating an optically-pumped linearly-chirped fiber Bragg grating," *IEEE Trans. Microw. Theory Technol.*, vol. 59, no. 12, pp. 3531–3537, Dec. 2011.
[19] J. W. Shi, F. M. Kuo, C. Nan-Wei, S. Y. Set, C. B. Huang, and J. E. Bowers, "Photonic generation and wireless transmission of linearly/ nonlinearly continuously tunable chirped millimeter-wave waveforms with high time-bandwidth product at W-band," *IEEE Photon. J.*, vol. 4, no. 1, pp. 215–223, Feb. 2012.
[20] C. B. Huang, D. E. Leaird, and A. M. Weiner, "Time-multiplexed photonically enabled radio-frequency arbitrary waveform generation with 100 ps transitions," *Opt. Lett.*, vol. 32, no. 22, pp. 3242–3244, 2007.
[21] C. B. Huang, D. E. Leaird, and A. M. Weiner, "Synthesis of millimeter-wave power spectra using time-multiplexed optical pulse shaping," *IEEE Photon. Technol. Lett.*, vol. 21, no. 18, pp. 1287–1289, Sep. 2009.
[22] A. Dezfooliyan and A. M. Weiner, "Photonic synthesis of high fidelity microwave arbitrary waveforms using near field frequency to time mapping," *Opt. Exp.*, vol. 21, no. 19, pp. 22974–22987, 2013.
[23] A. M. Weiner, "Femtosecond pulse shaping using spatial light modulators," *Rev. Sci. Instrum.*, vol. 71, no. 5, pp. 1929–1960, 2000.
[24] A. M. Weiner, "Ultrafast optical pulse shaping: A tutorial review," *Opt. Commun.*, vol. 284, no. 15, pp. 3669–3692, 2011.
[25] M. A. Muriel, J. Azana, and A. Carballar, "Real-time Fourier transformer based on fiber gratings," *Opt. Lett.*, vol. 24, no. 1, pp. 1–3, 1999.
[26] V. Torres-Company, D. E. Leaird, and A. M. Weiner, "Dispersion requirements in coherent frequency-to-time mapping," *Opt. Exp.*, vol. 19, no. 24, pp. 24718–24729, 2011.
[27] A. M. Weiner, *Ultrafast Optics*. New York, NY, USA: Wiley, 2009.
[28] N. Levanon and E. Mozeson, *Radar Signals*. New York, NY, USA: Wiley, 2004.
[29] N. Levanon, *Radar Principles*. New York, NY, USA: Wiley 1988.
[30] D. Jackson, R. Priest, A. Dandridge, and A. Tveten, "Elimination of drift in a single-mode optical fiber interferometer using a piezoelectrically stretched coiled fiber," *Appl. Opt.*, vol. 19, no. 17, pp. 2926–2929, 1980.
[31] V. R. Supradeepa, C. M. Long, D. E. Leaird, and A. M. Weiner, "Fast characterization of dispersion and dispersion slope of optical fiber links using spectral interferometry with frequency combs," *IEEE Photon. Technol. Lett.*, vol. 22, no. 3, pp. 155–157, Feb. 2010.
[32] D. R. Cox and D. V. Hinkley, Theoretical Statistics. London, U.K.: Chapman & Hall, 1974.
[33] Y. Li, A. Dezfooliyan, and A. M. Weiner, "Photonic synthesis of spread spectrum radio frequency waveforms with arbitrarily long time apertures," *IEEE J. Lightw. Technol.*, Special issue on Microwave Photonics, to be published, 2014.

Amir Rashidinejad received the B.Sc. degree in electrical engineering from Sharif University of Technology, Tehran, Iran, in 2011. He is currently working toward the Ph.D. degree in the School of Electrical and Computer Engineering, Purdue University, West Lafayette, IN, USA. His current research interests include microwave-photonics, microwave and millimeter-wave arbitrary waveform generation, and applications in ranging and communication systems.

Andrew M. Weiner received the Sc.D. degree in electrical engineering from the Massachusetts Institute of Technology, Cambridge, MA, USA, in 1984. After Sc.D. degree he joined Bellcore, at that time a premier telecommunications industry research organization, first as a Member of Technical Staff and later as a Manager of Ultrafast Optics and Optical Signal Processing Research. He is currently the Scifres Family Distinguished Professor of Electrical and Computer Engineering. In 2008, he was elected to membership in the National Academy of Engineering and in 2009 was named a Department of Defense National Security Science and Engineering Faculty Fellow. He recently served a three year term as the Chair of the National Academy's U.S. Frontiers of Engineering Meeting; at present, he serves as an Editor-in-Chief of *Optics Express*, an all-electronic, open access journal publishing more than 3000 papers a year emphasizing innovations in all aspects of optics and photonics. He joined Purdue as a Professor in 1992, and has since graduated more than 30 Ph.D. students. He has also spent sabbaticals at the Max Born Institute for Nonlinear Optics and Ultrashort Pulse Spectroscopy, Berlin, Germany, and at JILA, University of Colorado and National Institute of Standards and Technology, Boulder, CO, USA.

His research interests include ultrafast optics, with a focus on processing of extremely high speed lightwave signals. He is especially well known for his pioneering work on programmable generation of arbitrary ultrashort pulse waveforms, which has found application both in fiber optic networks and in ultrafast optical science laboratories around the world.

Prof. Weiner is author of a textbook entitled *Ultrafast Optics*, has published eight book chapters and more than 270 journal articles, and is the inventor of 15 U.S. patents. His numerous awards include the Hertz Foundation Doctoral Thesis Prize in 1984, the Optical Society of America's Adolph Lomb Medal in 1990 and R.W. Wood Prize in 2008, the International Commission on Optics Prize in 1997, and the IEEE Photonics Society's William Streifer Scientific Achievement Award in 1999, and Quantum Electronics Prize in 2011. At Purdue, he has been recognized with the inaugural Research Excellence Award from the Schools of Engineering in 2003, the Provost's Outstanding Graduate Student Mentor Award in 2008, and the Herbert Newby McCoy Award for outstanding contributions to the natural sciences in 2013.